

RESEARCH ARTICLE

NWP calibration applied to Aeolus Mie channel winds

Gert-Jan Marseille¹  | Jos de Kloe¹ | Uwe Marksteiner² | Oliver Reitebuch² | Michael Rennie³ | Siebren de Haan¹

¹Royal Netherlands Meteorological Institute (KNMI), De Bilt, The Netherlands

²Deutsches Zentrum für Luft- und Raumfahrt (DLR), Institut für Physik der Atmosphäre, Oberpfaffenhofen, Germany

³European Centre for Medium-Range Weather Forecasts, Reading, UK

Correspondence

G.-J. Marseille, KNMI, PO Box 201, 3730 AE De Bilt, The Netherlands
Email: gert-jan.marseille@knmi.nl

Abstract

Aeolus is the first Doppler wind lidar (DWL) to measure wind profiles from space. Aeolus is an ESA (European Space Agency) explorer mission with the objective to retrieve winds from the collected atmospheric return signal which is the result of Mie and Rayleigh scattering of laser-emitted light by atmospheric molecules and particulates. The focus of this paper is on winds retrieved from instrument Mie channel collected data, that is, originating from Mie scattering by atmospheric aerosols and clouds. The use of simulated data from numerical weather prediction (NWP) models is a widely accepted and proven concept for the monitoring of the performance of many meteorological instruments, including Aeolus. Continuous monitoring of Aeolus Mie channel winds against model winds from the European Centre for Medium-Range Weather Forecasts (ECMWF) has revealed systematic errors in retrieved Mie winds. Following a reverse engineering approach, the systematic errors could be traced back to imperfections of the data in the calibration tables which serve as input for the on-ground wind processing algorithms. A new algorithm, denoted NWP calibration, makes use of NWP model winds to generate an updated calibration table. It is shown that Mie winds retrieved by making use of the NWP-based calibration tables show reduced systematic errors, not only when compared to NWP model winds but also when compared to an independent dataset of very-high-resolution aircraft wind data. The latter gives high confidence that the NWP-based calibration algorithm does not introduce model-related errors into retrieved Aeolus Mie winds. Based on the presented results in this paper, the NWP-based calibration table, as part of the level-2B wind processing, has become part of the operational processing chain since 01 July 2021.

KEYWORDS

Aeolus, Mie channel, NWP-based calibration, satellite wind profiling

1 | INTRODUCTION

Aeolus was launched in August 2018 by the European Space Agency (ESA) and is the first satellite mission to

provide wind profiles from space using a Doppler wind lidar (DWL). As such, Aeolus partly fills the wind data gap of the current global observing system (Baker *et al.*, 2014; Straume *et al.*, 2020). A spaceborne DWL has been

This is an open access article under the terms of the Creative Commons Attribution-NonCommercial-NoDerivs License, which permits use and distribution in any medium, provided the original work is properly cited, the use is non-commercial and no modifications or adaptations are made.

© 2022 The Authors. *Quarterly Journal of the Royal Meteorological Society* published by John Wiley & Sons Ltd on behalf of the Royal Meteorological Society.

considered for decades as the most promising technology to provide accurate wind profiles from space for weather and climate (Baker *et al.*, 1995; Stoffelen *et al.*, 2005). After the successful launch in 2018 and subsequent commissioning phase, Aeolus-measured winds have been used operationally at ECMWF since January 2020, followed by Deutsche Wetterdienst (DWD), Météo-France, the UK Met Office (UKMO) and the National Centre for Medium-Range Weather Forecasting (NCMRWF, India), all showing substantial positive impact of Aeolus winds when used in their global NWP systems (e.g., Rennie *et al.*, 2021). Given the success of Aeolus, investigations are ongoing to look forward to future vertical wind profiling capability (Stoffelen *et al.*, 2020) to fulfill the World Meteorological Organisation (WMO) Rolling Review of Requirements in operational meteorology (WMO, 2018).

The Aeolus DWL instrument, named ALADIN (Atmospheric LAsER Doppler INstrument), is operated in the ultraviolet part of the electromagnetic spectrum at 354.8 nm wavelength at 50.5 Hz pulse frequency. The instrument points at an angle of 35 degrees off-nadir toward the atmosphere to allow measurement of the horizontal wind component. Part of the emitted laser light is returned to the instrument by Rayleigh scattering from atmospheric molecules and Mie scattering from particulates (aerosol, cloud droplets and ice crystals). On the instrument receiver, the total return signal from molecules and particles is spectrally separated by a Fizeau interferometer (for the so-called Mie channel; aerosol/cloud), and two Fabry–Perot interferometers (the so-called Rayleigh channel; molecules). On-board hardware controls the range gating to separate the signals into height bins to yield a wind component profile. Aeolus has 24 vertical bins with sizes typically increasing with altitude, but limited to an integer times ~ 250 m, for example 500 m in the boundary layer (below 2 km altitude), 1 km in the free troposphere (2–16 km) and 1.5–2 km above 16 km altitude to allow a maximum altitude of about 30 km above the surface. Aeolus vertical sampling is flexible in that the range bin settings can be changed on average eight times per orbit to optimize the sampling as a function of climate zone. For instance, tropical cirrus is found at altitudes up to about 18 km, while clouds are hardly found above 10 km altitude over polar regions, except for specific periods of polar stratospheric cloud presence. A more detailed description of ALADIN design of the laser transmitter, receiver optics and its performance in space during the first year of the mission is found in Lux *et al.* (2020; 2021).

On board, the return signal from typically 18 consecutive pulses is accumulated which corresponds to a distance of about 2.85 km along the satellite track. The resulting signal, called the measurement, is broadcast to the ground station and is the highest horizontal resolution

which Aeolus provides. Accumulation of measurements to observation level is part of the on-ground processing and software has been developed to be flexible on the accumulation length. Typical accumulation lengths for Mie and Rayleigh channel winds used during the operational phase of the mission are 11–15 km (4–5 measurements) and about 86 km (30 measurements), respectively. The resulting wind in each range bin along the laser beam line-of-sight (LOS) is projected to the horizontal to provide the HLOS wind (assuming mean vertical motion is negligible at observation length-scale) and a corresponding error estimate, based on the signal-to-noise (SNR) ratio of the accumulated signal, which can be used in NWP data assimilation systems.

An important component of the Aeolus mission is the on-ground processing to retrieve profiles of the HLOS wind component. The ground processing combines all available information downlinked by the satellite to the ground station. This information includes the spectral properties of the collected photons on the instrument receiver and instrument characterization from in-orbit instrument calibration activities, i.e., the spectral response calibration (ESA, 2008; Tan *et al.*, 2008; Reitebuch, 2012). At a high abstraction level one can capture this process by the following formula:

$$H = F(\text{collected photons, calibration}), \quad (1)$$

with F denoting the on-ground processing software and H the HLOS wind component following the convention in Rennie *et al.* (2021).

Continuous monitoring of Mie channel winds against ECMWF model winds has revealed systematic errors in retrieved Mie winds which could be traced back to imperfections of the data in the calibration tables. The latter serve as input for the level-2B (L2B) processing, that is, the retrieval of HLOS wind profiles. These imperfections can be explained by the fact that the emitted laser energy and optical efficiency of the instrument are lower than anticipated before launch, meaning that the SNR ratio of the received signal is lower than anticipated before launch. As a consequence the in-orbit instrument response calibration (IRC) strategy is limited to regions with strong surface returns, hence high albedo, that is, the polar regions. Cloud coverage over the poles often prevents the laser beam from reaching the surface, which further limits calibration capabilities. Another issue with the IRC is the size of the frequency steps (25 MHz) which is too large to nicely capture the nonlinearities of the Mie spectral response, discussed in the next section. These limitations and resulting imperfections in the IRC data, which propagate into retrieved Mie winds as systematic errors, could not be fully solved until August 2021, but investigations are ongoing.

For this reason, an alternative approach is presented in this paper which makes use of model-simulated winds at Aeolus wind locations to characterize (calibrate) the instrument with focus here on Mie channel winds.

The next section discusses the processing steps to retrieve Mie winds as part of the L2B-processor (L2Bp). In Section 3 the principle of NWP calibration and its application to Mie winds is discussed. The dataset used to assess NWP calibration and results are discussed in Sections 4 and 5 respectively, which will show that the application of NWP calibration provides improved Mie winds compared to the (then) operational product which is based on calibration tables from in-orbit instrument response calibrations. A summary and discussion is provided in Section 6.

2 | MIE WIND PROCESSING

As part of the receiver of ALADIN, the atmospheric return signal from particles is imaged onto the Mie spectrometer (Fizeau interferometer) and then integrated over the 16 columns of the accumulation charge coupled device (ACCD; Reitebuch, 2012; Reitebuch *et al.*, 2018), which covers a spectral range of about $(-800, 800)$ MHz corresponding to a LOS wind range of about $(-142, 142)$ m·s⁻¹ and a HLOS range of about $(-223, 233)$ m·s⁻¹. Besides emitting laser light toward the atmosphere, part of the emitted pulse is internally diverted toward the spectrometer. The Mie fringe is approximated by a Lorentzian function. The location of the peak on the ACCD is obtained from fitting the measured signal on the ACCD to a Lorentzian curve using the Mie Core downhill simplex algorithm (Reitebuch *et al.*, 2018). This is applied to both the internal reference and atmospheric measured spectrum to compensate for laser frequency fluctuations. The difference between the two peak locations defines the actual Doppler frequency shift induced by scattering of laser-emitted light on atmospheric particles, which move with the ambient wind. The Doppler frequency shift, Δf , is proportional to the speed v_{LOS} of the moving targets along the laser beam LOS:

$$v_{\text{LOS}} = -\frac{\lambda}{2}\Delta f, \quad (2)$$

with λ denoting the laser wavelength with a value of 354.8 nm.

Application of Equation (2) requires conversion of the estimated peak locations to frequency space. This is done by means of a Mie response calibration (MRC) curve which relates peak pixel location to frequency. These calibration curves are the result of an IRC for which data are obtained when Aeolus is operated in calibration mode, that is, by pointing the instrument telescope to the Earth surface at an angle close to nadir to avoid large horizontal wind

speeds due to, for example, blowing snow or sand. In calibration mode, Aeolus cannot make wind observations. Two (MRC) calibration curves are derived, one for the atmospheric path (from ground returns basically) and one for the internal reference path. A more in-depth description of the Mie channel calibration strategy is found in section 3.4.2 of Marksteiner (2013) and chapters 8 and 9 of Reitebuch *et al.* (2018). Both MRC curves, denoted R , from the atmospheric (atm) and internal reference (int) paths are close to linear with a small, but non-negligible, nonlinear contribution on top:

$$R_x(f) = \alpha_x + \beta_x f + \gamma_x(f), \quad (3)$$

with f denoting the frequency offset (Hz), slope β the so-called mean sensitivity, α the intercept value at zero frequency offset and γ the nonlinearity contribution to the Mie response and subscript x denoting the two calibration paths: $x = \{\text{atm}, \text{int}\}$. The contribution of the nonlinearity is fundamental and can be attributed to the following main causes:

- (i) the ACCD does not sample the full Mie fringe profile which causes “edge effects” when the Mie fringe is close to the edge of the useful spectral range,
- (ii) the coarse resolution of the ACCD, where one pixel samples about 100 MHz, and nonlinearity of the Mie spectral shape results in a nonlinear function over the width of a pixel, and
- (iii) the illumination of the Fizeau interferometer is not equal in the optical round aperture (this is true especially for the internal path). This leads to different illumination of some parts of the spectral range, and thus a deviation from a pure Lorentzian (or Airy) function.

All three effects are basically corrected with the Mie nonlinear correction function γ in Equation (3) which needs characterization in orbit, via the MRC. More details on the nonlinearity contributors are found in Reitebuch *et al.* (2018).

The values of the parameters in Equation (3) have been collected in calibration tables which serve as input for the L2Bp. The correction for the nonlinear contribution to the response has been implemented in pixel space as a look-up table of response correction (also denoted residual) values $\Delta R_x(i)$ with index i for corresponding response values $R_x(i)$. Given the value of R_x , the corresponding nonlinear correction, ΔR_x is obtained from linear interpolation of the table values. For the atmospheric signal, the values of the look-up table for the MRC nonlinearity for a particular calibration file are visualized by the blue curve in Figure 1.

When operated in wind mode, the atmospheric return signal is imaged onto the Mie detector ACCD and the

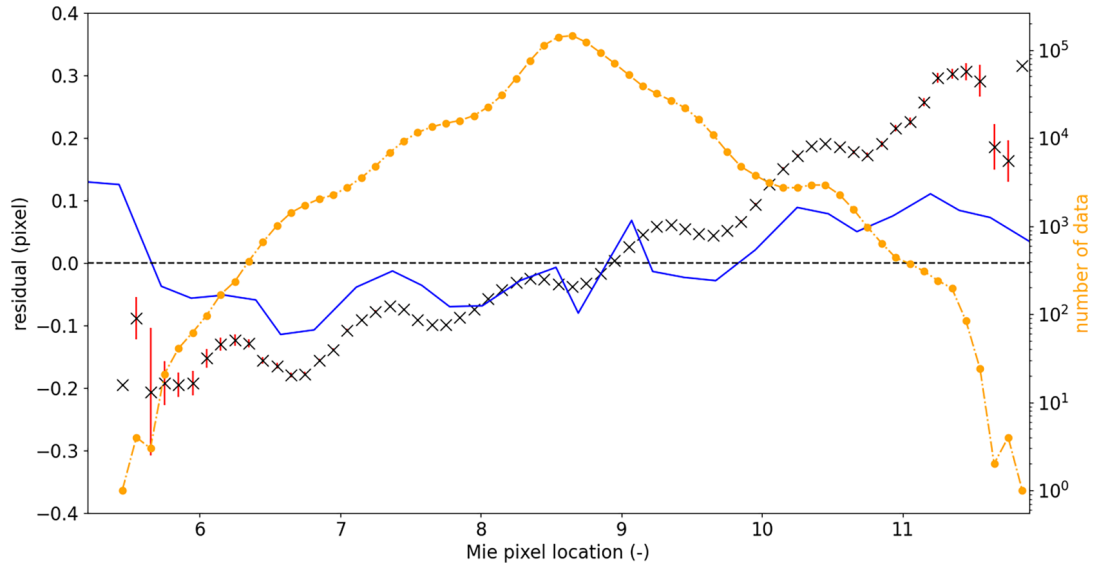


FIGURE 1 Mie spectral response nonlinearity (residual from linear fit) as a function of Mie pixel location, P_{mie} , as obtained from 16 September 2019 in orbit IRC#48, denoted γ_{atm} (blue), and as obtained from NWP calibration, that is, from $(P_{mie} - P_{NWP})$ and denoted γ_{NWP} (black crosses), which was derived from one month (December 2019) of Aeolus data. The orange dots denote the number of data available within the 0.1 sized pixel bins. The red error bar denotes the standard deviation of the values within the bin divided by the square root of the number of data in the bin to reflect the standard deviation of the mean value. The size of the error bar is negligible for most pixel bins

Mie peak location, denoted P_{mie} , is estimated as described above from Lorentzian curve fitting. In addition, a small part of the emitted laser light is separated and imaged onto the Mie detector ACCD beforehand which provides the internal reference peak location, denoted P_{ref} . The corresponding frequency offsets are then obtained from Equation (3) and the implementation of the MRC nonlinearity contribution:

$$f_{mie} = \{P_{mie} - \alpha_{atm} - \Delta R_{atm}(P_{mie})\} / \beta_{atm}, \quad (4)$$

$$f_{ref} = \{P_{ref} - \alpha_{int} - \Delta R_{int}(P_{ref})\} / \beta_{int}. \quad (5)$$

The Doppler shifted frequency, Δf , is obtained from the difference of Equations (4) and (5), which is converted to wind space through Equation (2):

$$v_{LOS} = -\frac{\lambda}{2}(f_{mie} - f_{ref}) = v_{mie} - v_{ref}. \quad (6)$$

In addition, corrections are needed, for example, to correct for contributions of the spacecraft velocity to the LOS wind (pointing errors) and ALADIN's telescope primary (M1) mirror temperature variations (Weiler *et al.*, 2021). These corrections are determined from algorithms outside the L2Bp and used as input parameters to the L2Bp. The sum of these corrections to the LOS is denoted here by v_{corr} . The corrected Mie LOS wind velocity, \tilde{v}_{LOS} , is obtained from

$$\tilde{v}_{LOS} = v_{LOS} - v_{corr}. \quad (7)$$

Finally, \tilde{v}_{LOS} is projected to the horizontal to yield the HLOS wind component, denoted H , following the convention in Rennie *et al.* (2021):

$$H = \tilde{v}_{LOS} / \sin(\theta), \quad (8)$$

with θ denoting the local incidence angle at the observation location. Note that Equations (7 and 8) are in agreement with Equation (13) from Tan *et al.* (2008). The HLOS wind component in Equation (8) is denoted Mie-cloudy wind and is part of the Aeolus L2B product (besides the Rayleigh channel “clear air” derived winds) disseminated to the NWP community. It is noted that almost all of the Aeolus Mie observations are from cloudy returns and only a very limited fraction from aerosol returns. For this reason Mie winds are also denoted Mie-cloudy winds in the remainder of this paper.

3 | NWP CALIBRATION APPLIED TO MIE WINDS

The use of NWP model data has proven to be very useful for monitoring instrument performances, including those from satellites (Rennie and Isaksen, 2020). In addition, NWP model data have proven to be useful to detect instrumental imperfections and to develop schemes to correct for these imperfections by making use of NWP model data (e.g., applied to satellite radiance data; Eyre, 1992)

but many other examples exist in the scientific meteorological literature and some have been integrated in data assimilation systems, for example through variational bias correction (VARBC) schemes. The most striking example of making use of NWP model data in data processing in the context of Aeolus are the temperature variations of the telescope primary (M1) mirror. It was found that the temperature gradient over the telescope correlates very well with observations-minus-background ($o - b$) statistics (Section 5 gives a more detailed explanation), in particular for Rayleigh channel-derived winds (Rennie and Isaksen, 2020). This information was used to develop a correction scheme, based on NWP model data, which reduces biases in Rayleigh winds to a level acceptable for use in data assimilation as part of NWP (Weiler *et al.*, 2021). It is noted that NWP winds are accurate enough in a global average and large time period sense to apply such correction schemes. In particular the ECMWF model comparison against radiosonde winds shows a bias typically less than $0.3 \text{ m}\cdot\text{s}^{-1}$ for the zonal wind component (Weiler *et al.*, 2021).

One step further is the use of NWP model data as part of the processing chain to retrieve the geophysical product. Examples can be found for the abovementioned satellite radiance data but also in scatterometry where measurements of ocean surface roughness are converted to wind speed and direction at 10 m height. The processing results in ambiguous solutions and an ambiguity removal scheme, based on NWP model data, is often used to select the correct wind solutions. In the context of Aeolus, NWP model temperature and pressure information is used as part of the Rayleigh channel wind processing (Tan *et al.*, 2008).

Yet another step further is the use of NWP data to gain information on the process steps which have resulted in the final product, also known as reverse (or back) engineering. The NWP calibration method discussed here fits this concept. As summarized in Equation (1), calibration is an important component of the process to yield the final product – the Mie channel HLOS wind component in this case. As will be shown in Section 5, systematic errors in retrieved Mie winds could be traced back to imperfections in the calibration tables which are used in the L2Bp. With reverse engineering, NWP model data are used to correct or replace the calibration tables and can thus be regarded as the inverse of Equation (1):

$$\text{calibration} = F^{-1}(\text{collected photons}, H_{\text{NWP}}), \quad (9)$$

with H_{NWP} denoting the HLOS wind component as obtained from NWP model fields at the Aeolus observation location. With NWP calibration the procedure in Section 2 is performed in reverse order starting from the zonal, u , and meridional, v , wind components at the

Aeolus observation location as provided by a NWP model; Equation (10). Here we used the u and v derived from the auxiliary meteorological dataset (AUX_MET), which is a short-range ECMWF global model forecast run of typically up to 12 hr at Tco1279 resolution ($\sim 9 \text{ km}$ grid) along Aeolus predicted ground-tracks. The azimuth angle, ψ , is defined as the angle (clockwise) between the laser beam direction and geographical north and is available to the L2Bp from the input files. The LOS wind component follows from Equation (8). The resulting value represents the corrected LOS velocity of Equation (7). To arrive at the (uncorrected) Mie LOS velocity, v_{mie} , the contributions of the internal reference and needed corrections are added following Equations (6 and 7). The resulting uncorrected Mie LOS velocity, v_{mie} , is next converted to frequency space through division by $-\lambda/2$, following Equation (2), to yield f_{mie} . In formulae the above steps read:

$$H_{\text{NWP}}(u, v) = -u \sin(\psi) - v \cos(\psi), \quad (10)$$

$$\tilde{v}_{\text{LOS}} = H_{\text{NWP}}(u, v) \sin(\theta), \quad (11)$$

$$v_{\text{mie}} = \tilde{v}_{\text{LOS}} + v_{\text{ref}} + v_{\text{corr}}, \quad (12)$$

$$f_{\text{mie}} = v_{\text{mie}} / (-\lambda/2). \quad (13)$$

Setting γ_{atm} equal to zero in Equation (4) and rearranging terms yields:

$$P_{\text{NWP}} = f_{\text{mie}} \beta_{\text{atm}} + \alpha_{\text{atm}}, \quad (14)$$

with P_{NWP} denoting the atmospheric path peak location on the Mie channel ACCD which would have been measured by Aeolus in the case of a perfect instrument, and the model wind would equal the true atmospheric wind. It is noted that the corresponding fitted peak location P_{mie} is the result of actual measured data and L2B processing and inherently *does* contain the nonlinearity contribution of the instrument (that is, Equation (3), to the linear part of the Mie spectral response. On the other hand, P_{NWP} has been obtained by explicitly ignoring the nonlinearity contribution of the Mie response by assuming a perfect linear Mie spectral response in Equation (14). The difference between P_{mie} and P_{NWP} thus reflects the sum of the instrument nonlinearity part of the Mie spectral response plus instrument noise (on top of P_{mie}) plus NWP errors (on top of P_{NWP}). The hypothesis is that the contributions of the latter two will vanish when averaging over a large sample of data (many orbits). If that can be shown, then the described procedure will provide the actual instrumental nonlinearity part of the MRC, denoted γ_{NWP} , which may be compared to γ_{atm} obtained from the IRC (atmospheric path) and as used in Equation (3) as part of the operational

TABLE 1 Values for the linear part of the Mie spectral response calibration curves. β (sensitivity) and α (intercept at zero frequency) appear in Equation (3)

MRC	β (ACCD pixel/GHz)	α (ACCD pixel index)
atm	9.256000	43.251434
int	9.593655	44.146213

The values are obtained from the Mie response calibration XML formatted file, with filename mentioned in footnote 1, obtained from IRC#48 performed in orbit on 16 September 2019. According to the date/time stamps in the filename, this calibration file was valid for the December 2019 period under investigation. MRC = Mie response calibration; ACCD=accumulation charge coupled device; atm=atmospheric path; int=internal reference path.

processing chain. The next section gives an example and a visual presentation of the above discussion.

4 | DATASET

The procedure described in the previous section has been applied to one month of Aeolus data: December 2019. For the retrieval of HLOS wind profiles L2Bp version 3.40.2 was used, which was operational during the period 08 October–10 December 2020 and compatible for the processing of data obtained before this period. As input for the L2Bp, the L1B dataset from the first reprocessing activity, denoted baseline 1B10, which covered the period June–December 2019, was used. Calibration tables used are from calibration activities performed in orbit on 16 September 2019, numbered IRC#48 which was active for the reprocessing activity in December 2019. The resulting numbers from the calibration activity have been collected in an XML formatted file¹. The numbers in this file were used as part of the level-1B processing (L1Bp) to generate the L1B wind product file which serves as input for the L2Bp. The relevant calibration parameters and values for the linear part of the (MRC) have been summarized in Table 1.

The nonlinearity part of the atmospheric path of the MRC, γ_{atm} , as obtained from the XML file is shown as the blue curve in Figure 1. The procedure described in Section 3 provides an alternative nonlinearity estimate from NWP calibration, denoted γ_{NWP} . As explained in Section 3, each location of retrieved Mie wind provides a pair of $(P_{\text{mie}}, P_{\text{NWP}})$ with their difference $(P_{\text{mie}} - P_{\text{NWP}})$ largely reflecting the nonlinearity part of the MRC. The one-month period December 2019 provides 1.2 million pairs and corresponding differences which are binned in

0.1 sized pixel bins over the complete range of observed peak values. For each bin, the mean value of the differences is calculated and visualized as black crosses in Figure 1 with the red error bars denoting the one-sigma uncertainty. Clearly, the uncertainty of the estimated values increases near the smallest and largest pixel values which are related to rare extreme wind speeds.

The curvature of the black crosses shows an approximately linear trend with a one pixel periodic oscillation on top. This suggests that the sensitivity parameter for the atmospheric path in Table 1 slightly underestimates the actual instrument sensitivity. Then the actual instrumental nonlinearity is largely a periodic oscillation.

5 | RESULTS

As stated and motivated in Rennie *et al.* (2021), a state-of-the-art data assimilation system and forecast model (such as from ECMWF) is a powerful tool for monitoring and evaluating new observing systems. The forward modelled observation equivalent, denoted ‘*b*’ (also known as background, which is a short-term model forecast) can be compared to the observation, denoted ‘*o*’. Departure (or innovation) $(o - b)$ statistics provide valuable information on the quality of the observations, aside from being a crucial component in the analysis equations to yield the model forecast initial state (also known as the analysis) as part of the data assimilation step in NWP. Figure 2a shows $(o - b)$ statistics of the re-processed product which has similar systematic error characteristics as the operational Mie-cloudy wind product. As such, Figure 2a is representative for $(o - b)$ statistics of the operational product, which makes use of the inputs on sensitivity and intercept from Table 1 and of the MRC nonlinearity blue curve of Figure 1 as part of the processing in L2Bp. The statistics include a total of 1.2 million observations. A prerequisite for observations to have a positive impact in the analysis and subsequent forecasts is that their biases are small relative to the random error, that is, $E(o - b)$ should be close to zero with E denoting the expectation operator. The overall bias from all observations is small with a value of $-0.22 \text{ m}\cdot\text{s}^{-1}$. For the quantification of the random error of $(o - b)$ two measures have been used: standard deviation and scaled median absolute deviation (MAD²). The latter is less sensitive to outliers and equals the standard deviation in case of a Gaussian distributed $(o - b)$ and a scaling factor of 1.4826. Mie winds are rejected through quality control (QC) from the statistics if the estimated error,

¹The XML formatted file is named AE_OPER_AUX_MRC_1B_20190722T000059_20200101T235959_0001.EEF

²https://en.wikipedia.org/wiki/Median_absolute_deviation; accessed 14 January 2022

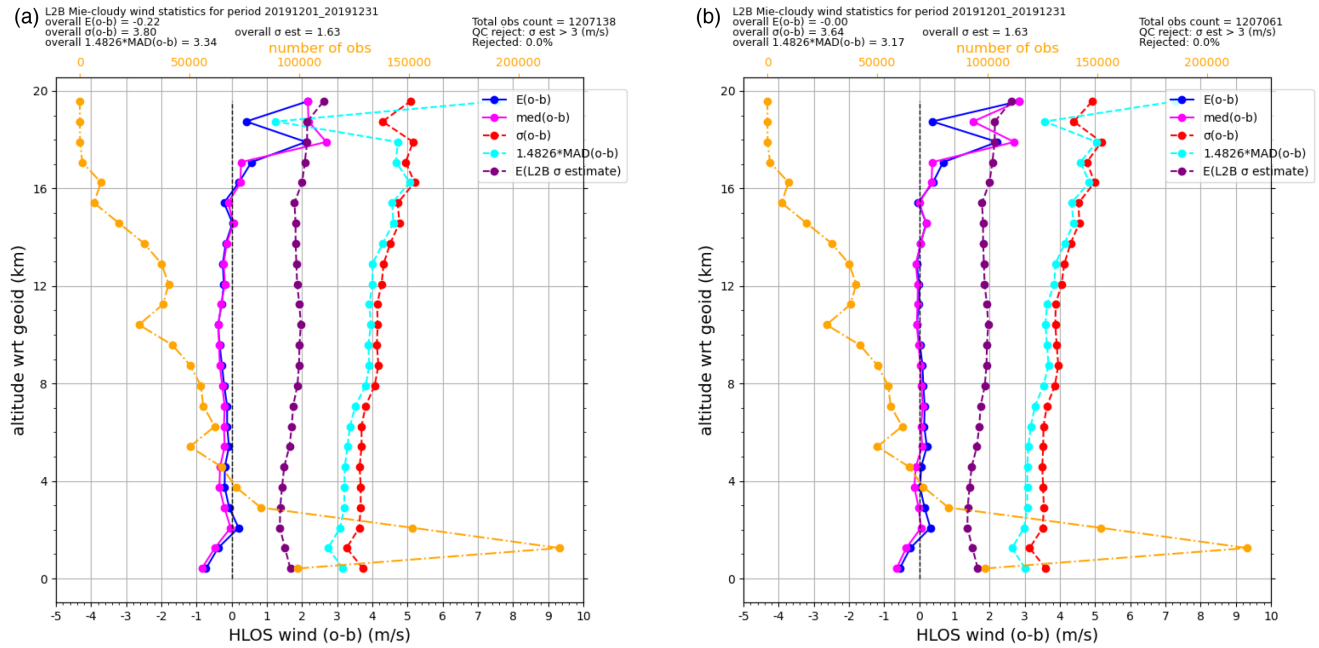


FIGURE 2 Mie-cloudy ($o - b$) statistics versus altitude for the one-month period December 2019, representative of (a) the operational L2B product and (b) with NWP calibration. The blue and magenta curves denote the mean and median ($o - b$) values respectively. The red and cyan curves represent the ($o - b$) random error, with red the standard deviation and cyan the scaled median absolute deviation (MAD); see the text for details. The purple line denotes the observation error as estimated by the L2Bp and is based on the SNR of the received Mie signal on the detector. The orange curve denotes the number of observations used in the statistics

which is an output parameter of the Mie wind processing scheme, exceeds a value of $3 \text{ m}\cdot\text{s}^{-1}$. For Figure 2a the resulting values of the ($o - b$) standard deviation and scaled MAD are 3.80 and $3.34 \text{ m}\cdot\text{s}^{-1}$ respectively with 0.0% winds rejected by QC. The overall estimated error equals $1.63 \text{ m}\cdot\text{s}^{-1}$. These values are representative for the Aeolus operational Mie-cloudy product for the December 2019 period.

Figure 2b shows similar statistics but now the L2Bp makes use of the NWP-based MRC nonlinearity curve denoted by the black crosses in Figure 1. As a result the overall ($o - b$) bias has vanished to $-0.00 \text{ m}\cdot\text{s}^{-1}$ and the ($o - b$) random error reduced to 3.64 and $3.17 \text{ m}\cdot\text{s}^{-1}$ for the standard deviation and scaled MAD respectively, a reduction of about 5% relative to operational Mie winds used in the left panel. The smoothness of the curve represented by the black crosses in Figure 1 implies that the random error of Mie-cloudy winds is left untouched when making use of the NWP-based MRC nonlinearity in the Mie wind processing. The fact that the overall bias of ($o - b$) has vanished completely does not come as a surprise because the NWP-based nonlinearity correction was constructed to do so. Also note that the same data used for the statistics in Figure 2b were also used for the construction of the NWP-based nonlinearity curve. The validity of the NWP-based nonlinearity curve for other periods depends on the stability of the instrument. The

nonlinearity characteristics of an instrument operating stably in time will not change much, which limits the need for regular updates of the NWP-based nonlinearity curve when used in the operational processing chain. This is further discussed in Sections 5.2 and 6. Mie-cloudy winds processed in the L2Bp with the NWP-based nonlinearity correction are denoted ‘corrected winds’ in the remainder, not to be confused with the correction used in Equation (7).

To investigate potential wind speed-dependent biases, Figure 3 presents a density scatter plot of Aeolus Mie-cloudy winds and the corresponding model background value. Close investigation of Figure 3a shows an artefact for near-zero wind speed for Mie-cloudy winds representative for the operational product. In addition, the distribution of points deviates from the diagonal for strong positive and negative winds, indicating an overestimate of Aeolus Mie-cloudy winds relative to corresponding model winds for high wind speeds. Figure 3b shows the result for the corrected Mie-cloudy product. In contrast to Figure 3a, the artefact at near-zero wind speed has been removed and in addition the scatter density is closer to the diagonal also for high wind speeds, indicating that the corrected Mie-cloudy winds are in better agreement with model winds for all wind regimes.

The artefact in Figure 3a becomes more prominent when considering ($o - b$) statistics versus wind speed as

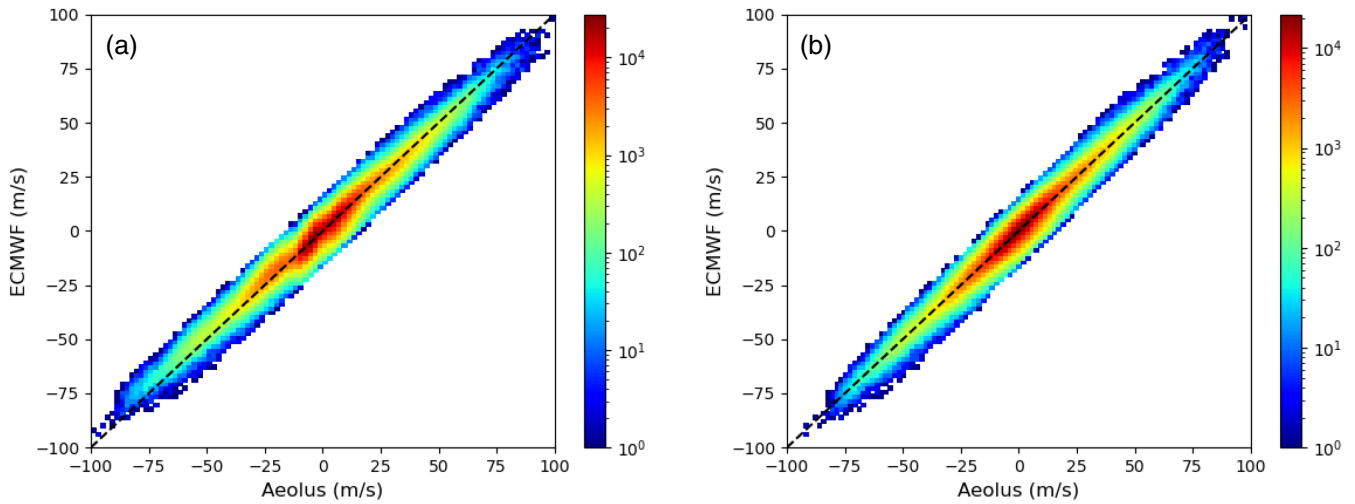


FIGURE 3 Density scatter plots of Aeolus Mie-cloudy winds along the x -axis and the ECMWF model equivalent along the y -axis for the one-month period December 2019 for (a) the operational L2B product and (b) when using the NWP-based MRC nonlinearity in the L2B processing. The black dashed line represents the diagonal

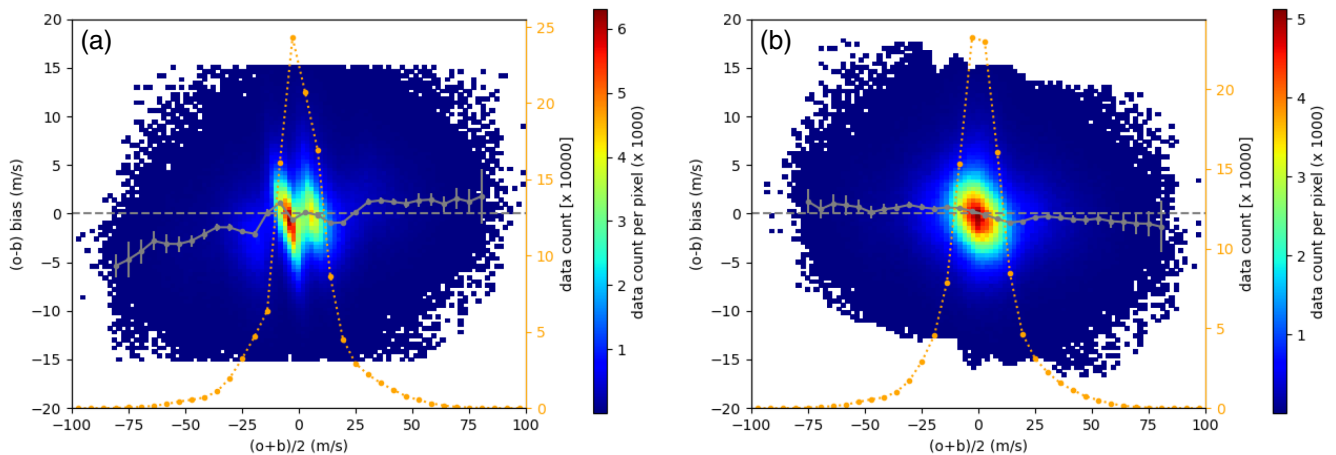


FIGURE 4 Mie-cloudy $(o - b)$ density as a function of true wind speed represented by $(o + b)/2$ for the one-month period December 2019 (a) representative of the operational L2B product and (b) based on NWP calibration. For the operational product Aeolus Mie-cloudy winds which deviate by more than $15 \text{ m}\cdot\text{s}^{-1}$ from the model are removed as part of the quality control procedure, which explains the clipping in (a). This QC was not applied to the corrected winds in (b) to maximize consistency of both datasets. The orange curve denotes the number of data points in each $5 \text{ m}\cdot\text{s}^{-1}$ bin. The grey curve (bias) shows the mean value in each bin with the error bar denoting the standard error

presented in Figure 4. Since the true wind speed is inherently unknown, there are several options for the wind speed to take along the x -axis: from o , from b or from a combination of both, for example, $(o + b)/2$. For Mie-cloudy winds, the amplitude of the random error compares well to the model wind error, which is estimated at $2\text{--}2.5 \text{ m}\cdot\text{s}^{-1}$ (Rennie *et al.*, 2021). Hence the random error of $(o + b)/2$ is smaller than of either o or b and selected here to represent the true atmospheric HLOS wind along the x -axis in Figure 4. Figure 4a clearly shows an artefact in the statistics for near-zero wind speed for the operational product which has disappeared for the corrected Mie-cloudy winds in (b). Yet, a wind speed-dependent slope is still

observed in (b). This is not a real wind speed-dependent bias but the result from what is called attenuation bias or regression dilution³ and can be explained by the fact that the independent variable along the x -axis is not the true (noise-free) atmospheric wind speed but a noisy representation of it. This effect was well demonstrated in Rennie (2016) assuming purely Gaussian noise for o and b . Then it can be demonstrated that fitting a linear regression curve to a scatter plot of (o, b) combinations and taking b as the independent variable results in a

³https://en.wikipedia.org/wiki/Errors-in-variables_models; accessed 14 January 2022

fitted curve with slope $1/(1 + \sigma_b^2/\sigma_t^2)$ with σ_b denoting the error standard deviation of the independent variable, the model background error in this case, and σ_t the standard deviation (spread) of the true atmospheric state which has been assumed Gaussian distributed with zero mean. Moreover, model error and true atmospheric spread are assumed uncorrelated, with σ_t substantially larger than σ_b . The estimated slope value, based on independent noisy data, is smaller than the actual value of 1, which applies for the relationship between o and the true atmospheric state, in case the latter would be available. This explains the expression: attenuation bias. As a result, the estimated slope of a scatter plot of $(o - b, b)$ combinations equals

$$s_b = \frac{1}{(1 + \sigma_b^2/\sigma_t^2)} - 1,$$

which is always less than or equal to zero.

A similar calculation taking o as the independent variable (along the x -axis and with b values along the y -axis) gives an estimated slope value of $1/(1 + \sigma_o^2/\sigma_t^2)$ with σ_o denoting the error standard deviation of the independent variable, the observation error in this case. As a result, the estimated slope of a scatter plot of $(o - b, o)$ combinations equals

$$s_o = 1 - \frac{1}{(1 + \sigma_o^2/\sigma_t^2)},$$

which is always greater than or equal to zero, hence of opposite sign compared to the slope when taking b as the independent variable. Indeed for σ_o or σ_b approaching zero, that is, when the independent variable approaches the true (noise-free) atmospheric state, the estimated slope values approach zero. Also, assuming independent errors in o and b , taking $(o + b)/2$ as the independent variable yields a slope value which is a weighted average of s_b and s_o , the weights determined by the squared standard deviation (variance) of o and b :

$$s_{ob2} = 0.5 \frac{(\sigma_b^2 s_b + \sigma_o^2 s_o)}{(\sigma_o^2 + \sigma_b^2)},$$

which is between the slope values when taking either o or b as the independent variable. For the special case of σ_o equal to σ_b , s_b equals $-s_o$ and the estimated slope s_{ob2} of the scatter plot for $(o - b, (o + b)/2)$ combinations equals zero.

The calculated values of the slope from the black regression curves in Figure 4 are 0.039 (3.9% slope error) and -0.014 (1.4% slope error) for (a) and (b) respectively. The positive 3.9% slope error in Figure 4a implies that the total (random plus systematic) observation error is substantially larger than the background error for the

operational Mie-cloudy product. The change from positive to negative -1.4% slope in Figure 4b implies a total observation error smaller than the background error for corrected Mie-cloudy winds. As there is no indication of reduced random errors between operational and corrected Mie-cloudy winds, this confirms that corrected Mie-cloudy winds have reduced systematic errors relative to the operational product – another indication that corrected Mie-cloudy winds are of better quality.

One can argue that using NWP model winds as part of the instrument calibration and next using the resulting calibration tables as part of the wind retrieval processing on the same Aeolus data may potentially draw retrieved winds toward the model wind or introduce model errors into retrieved winds, hence introducing a correlation between model errors and errors of retrieved winds. In current data assimilation systems, it is explicitly assumed that model and observation errors are uncorrelated. Introducing observations with correlated errors in the analysis is therefore potentially detrimental for the quality of the analysis and subsequent forecasts. It was substantiated before that there is no indication of reduced random errors for corrected Mie-cloudy winds. Corrected Mie-cloudy winds drawing too close to the model winds would show a sharp reduction in the overall $(o - b)$ random error relative to the uncorrected winds. The drop of the overall $(o - b)$ standard deviation by “only” 5% indicates that this is not the case. These findings are a strong indication that the overall global reduction of $(o - b)$ bias and standard deviation can be attributed to a reduction of the systematic error, in particular the wind speed dependent bias, as part of the total observation error of Mie-cloudy winds. To further elaborate on this hypothesis, Mie-cloudy winds are compared against an independent data source in the next section.

5.1 | Collocated Mode-S winds

In the recent decade, a new type of aircraft-related meteorological information has become available, which originates from observations inferred from a tracking and ranging radar used for air traffic control. This dataset is called Mode-S EHS because it is using the so-called Selective Enhanced Surveillance Mode of the radar. The meteorological information includes temperature and wind which can be derived from the position of the aircraft reported by heading, ground track, true air speed and Mach number (de Haan, 2011). Heading is the direction that the nose of the aircraft points to, true air speed is the speed of the aircraft with respect to air and the ground track is the motion of the aircraft relative to the ground. The wind vector is the difference between the motion of the aircraft

relative to the ground and its motion relative to the air (defined by the airspeed and heading). The interrogation frequency between aircraft and the traffic control radar is between 4 and 20 s, depending on the type of radar, meaning that profiles of wind and temperature can be inferred near airports during ascent and descent. At cruise level (approximately at 10 km altitude), with a typical aircraft speed of $250 \text{ m}\cdot\text{s}^{-1}$, atmospheric wind and temperature observations are obtained with 1–5 km spacing along the flight path. We used Mode-S EHS data from the European Meteorological Aircraft-Derived Data Center (EMADDC) at the Dutch weather service KNMI. A triple collocation study showed that the Mode-S wind component observation error is estimated to be less than $1.4 \pm 0.1 \text{ m}\cdot\text{s}^{-1}$ near the surface and around $1.1 \pm 0.3 \text{ m}\cdot\text{s}^{-1}$ at 500 hPa (de Haan, 2015). The data coverage of Mode-S in 2019 is mainly over the Netherlands, Belgium, Northern France, Germany and parts of the United Kingdom and Denmark, but has grown since then and the number of weather centres making use of the data in their operations is growing as well (e.g., Lange and Janjić, 2016). We note that the processing of Mode-S EHS wind data requires a heading correction from the magnetic North Pole, that is, the observation reference, to the true north (de Haan (2011)). For the used dataset, this correction is based on NWP model data from the limited-area model HIRLAM which is operational at KNMI. Given the different geographical domains, periods and models used for calibration of Mode-S EHS and Aeolus winds, we expect no correlation between corrections applied to Mode-EHS winds and Aeolus winds. As such, Mode-S EHS winds are considered as an independent data source for the validation of Aeolus winds.

For the December 2019 period, wind vector observations from Mode-S were converted to HLOS wind components (Equation (10)), and collocated with pairs of {Aeolus, ECMWF} HLOS winds, which are available from the Aeolus level-2B product. For each Aeolus Mie-cloudy wind observation, Mode-S observations were selected meeting the collocation criteria. These include

- (i) the horizontal distance between the observation locations is less than 100 km,
- (ii) the vertical distance is less than 250 m, and
- (iii) the time difference between observations is less than 30 min.

When more than one Mode-S observation passes the collocation criteria, the observation closest in space and time has been selected. For the December 2019 period this resulted in a total of 2,438 {Aeolus, ECMWF, Mode-S} collocation pairs for which geographical location and vertical distribution are displayed in Figure 5. The domain of Mode-S available observations in December 2019 is bounded by 0 and 17°E longitude and 45°N and 56°N latitude. From the vertical distribution of collocated observations in Figure 5b, most observations are found in the upper troposphere above 5 km altitude, but also many in the boundary layer between 1 and 2 km altitude.

Observation minus background statistics for Mode-S relative to ECMWF model winds in Figure 6a show a limited bias of $-0.12 \text{ m}\cdot\text{s}^{-1}$ and a standard deviation of $3.05 \text{ m}\cdot\text{s}^{-1}$, which is smaller on average than for Aeolus Mie-cloudy winds, whose statistics are in Figure 6b, c. These statistics are another confirmation of the good quality of Mode-S winds, thus proving their value as a high-quality independent data source. The statistics in

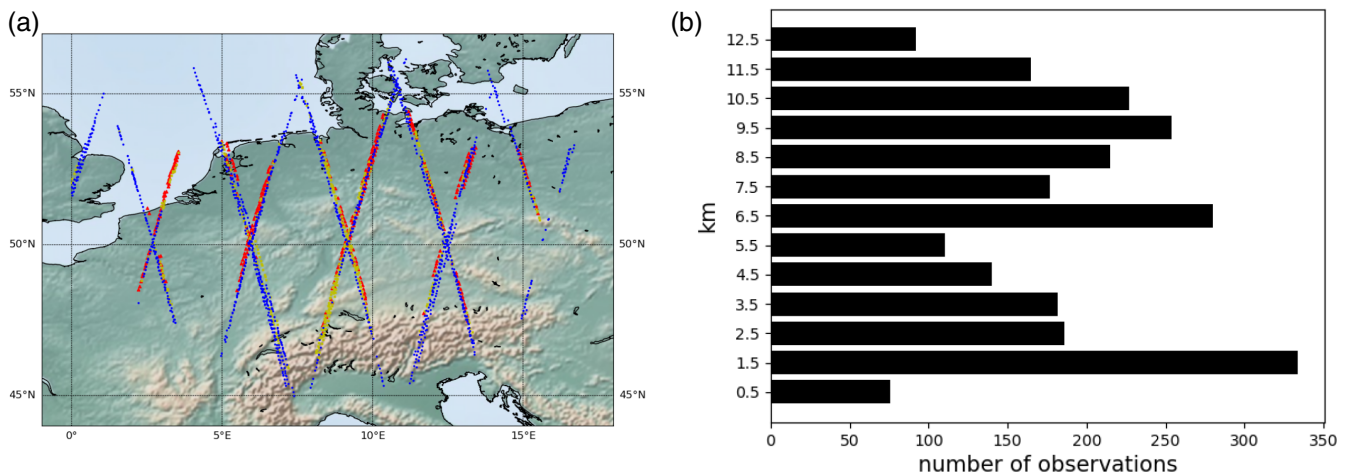


FIGURE 5 (a) shows Aeolus geolocations for which collocated Mode-S observations meet the collocation requirements in the December 2019 period; see text for details. Red, yellow and blue coloured locations denote observations taken in the boundary layer (below 2 km), lower troposphere (between 2 and 5 km) and upper troposphere (above 5 km), respectively. (b) shows the distribution of the 2,438 collocated observations with altitude

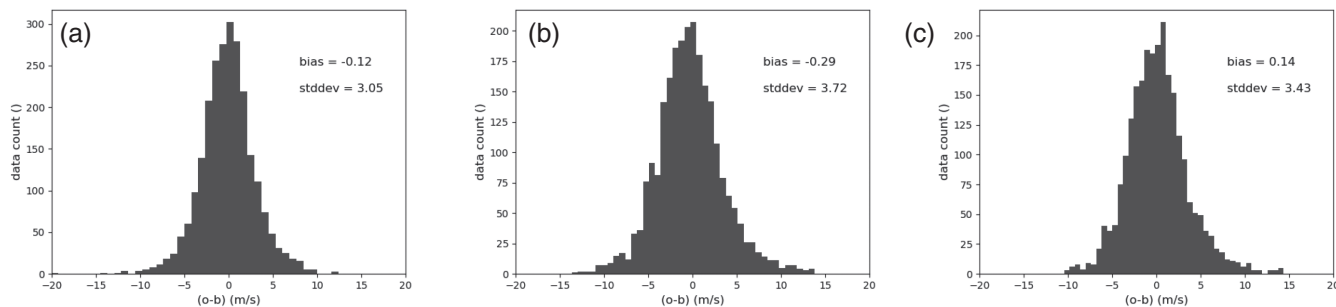


FIGURE 6 (a) HLOS wind observation minus background ($o - b$) statistics relative to ECMWF for Mode-S, (b) Aeolus Mie-cloudy representative for the operational product and (c) corrected Aeolus Mie-cloudy, based on NWP calibration, for the dataset of 2,438 collocated observations with locations displayed in Figure 5

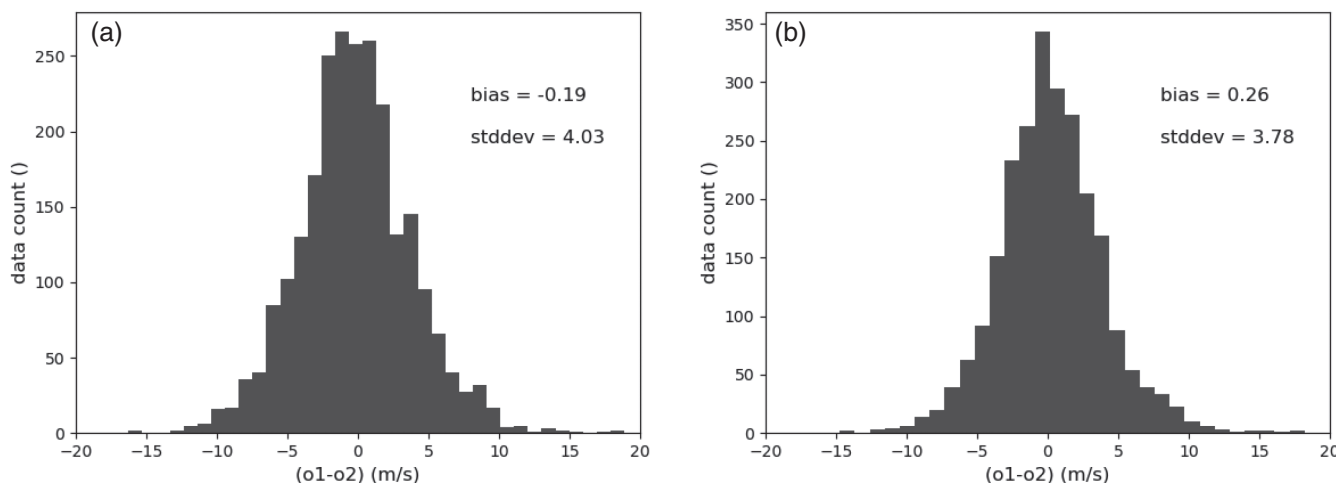


FIGURE 7 ($o_1 - o_2$) statistics similar to Figure 6 but now for two observation datasets: Aeolus Mie-cloudy HLOS winds are taken for ' o_1 ' and collocated Mode-S HLOS winds for ' o_2 '. (a) shows Mie-cloudy winds representative for the operational product and (b) the corrected winds based on NWP calibration

Figure 6 are based on the collocated dataset {Aeolus, ECMWF, Mode-S}. Here we note that as a consequence Mode-S and ECMWF model winds are not perfectly collocated in space but rather separated by the distance of the Mode-S observation closest to the Aeolus location within the collocation criteria defined above. This results in a slightly increased error in $(o - b)$ as compared to the use of spatially perfectly collocated model winds, as is done for Aeolus winds. The statistics of operational Aeolus Mie-cloudy winds in Figure 6b are slightly worse than the corrected Mie-cloudy winds in (c) with a smaller absolute $(o - b)$ bias of 0.29 versus $0.14 \text{ m}\cdot\text{s}^{-1}$ and smaller $(o - b)$ random error standard deviation of 3.72 versus $3.43 \text{ m}\cdot\text{s}^{-1}$, a reduction of almost 8%. These improvements are in the same order of magnitude as for earlier presented global statistics in Figure 2.

Figure 7 shows statistics of the direct comparison of Aeolus Mie-cloudy and Mode-S winds. Despite the relatively small sample, these results indicate that corrected Mie-cloudy winds obtained from the NWP-based

calibration tables are in better agreement with Mode-S winds than the Mie-cloudy winds representative for the operational product, with a substantial reduction of about 6% of the $(o - b)$ random error standard deviation from 4.03 to $3.78 \text{ m}\cdot\text{s}^{-1}$, and a slight increase of the absolute bias of $0.07 \text{ m}\cdot\text{s}^{-1}$.

Figures 3 and 4 showed artefacts in the o versus b and $(o - b)$ density scatter plots, suggesting systematic errors in either the observations or the model. Based on those results only, it cannot be concluded which data source is responsible for the systematic error. Mode-S winds are used as independent referee here. Figure 8 is similar to Figure 3. Figure 8a compares Mie-cloudy winds against Mode-S winds and shows a similar wiggling effect as was observed in Figure 3a. This is a strong indication that the systematic error causing the wiggling effect in the statistics is from Mie-cloudy winds. From Figure 8b, not only has this systematic error wiggling effect been removed for Mie-cloudy winds based on NWP calibration, but in addition the wind extremes are in better agreement with

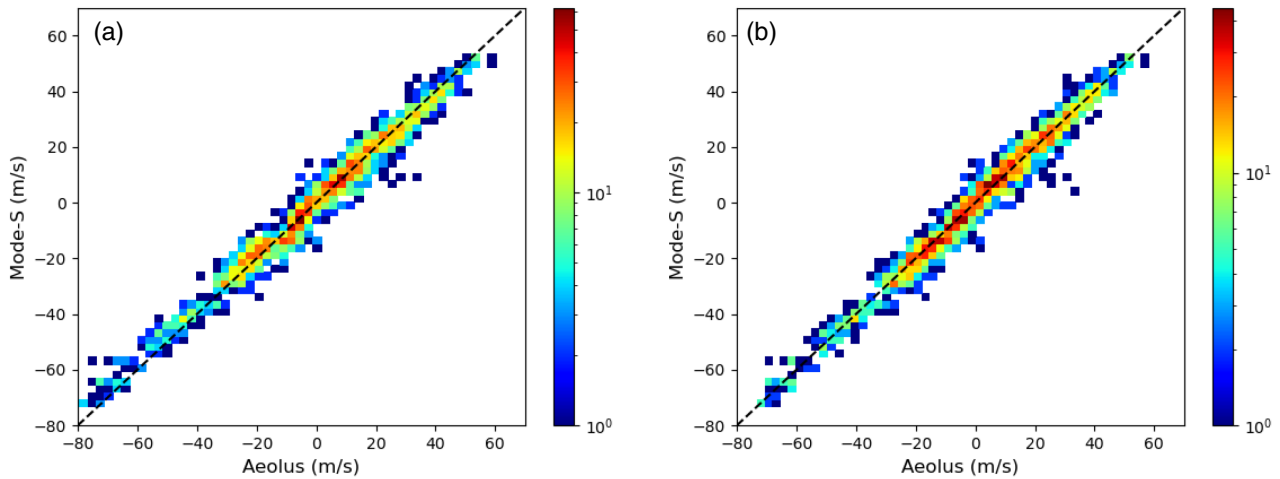


FIGURE 8 Density scatter plots of HLOS winds from Aeolus Mie-cloudy along the x -axis and Mode-S along the y -axis for the one-month period December 2019, (a) for the operational Aeolus L2B product and (b) when using the NWP-based calibration tables in the L2B processing. The black dashed line represents the diagonal

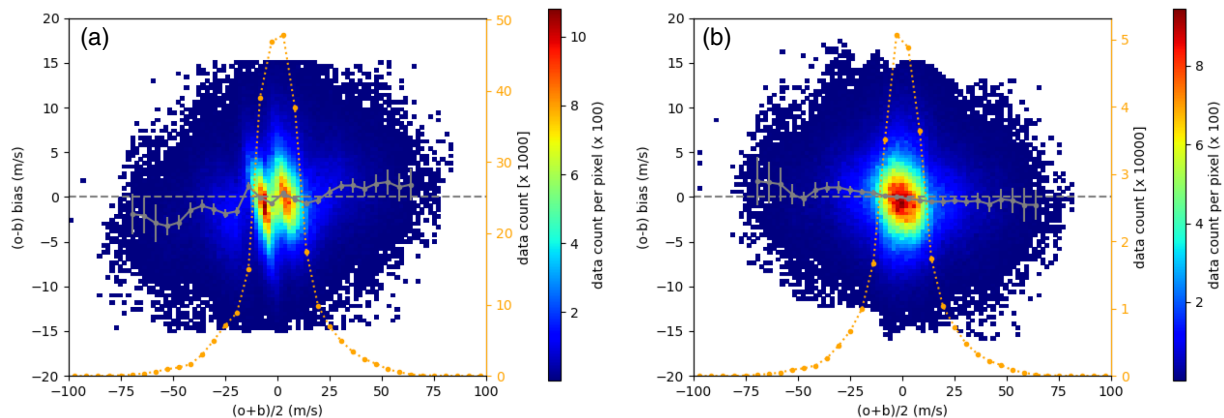


FIGURE 9 As Figure 4 but with Mie-cloudy $(o - b)$ statistics for the week 01–07 November 2019, (a) representative for the operational L2B product and (b) based on NWP calibration, the latter by making use of the Mie nonlinearity correction derived from Aeolus data from December 2019, that is, the black crosses in Figure 1

Mode-S winds, from comparing the lower left corners of both panels in Figure 8.

Despite the relatively small sample of 2,438 {Aeolus, ECMWF, Mode-S} collocations, the results presented in this section confirm earlier findings based on the global evaluation of {Aeolus, ECMWF} collocations presented in previous sections.

5.2 | Application in the operational context

Stability of the nonlinear characteristics of the Mie spectral response is a crucial aspect in the decision to introduce the NWP-based calibration table, derived in the previous section, as part of the operational Level-2B processing. Drifting nonlinear characteristics of the Mie spectral

response would reduce the quality of operationally produced Mie-cloudy winds with time and require a frequent update of the calibration table. Currently there is no procedure in the processing chain to automatically update the NWP-based calibration table, so this would require a time-consuming manual intervention, including the generation of new table values and testing their validity before deciding on operational implementation. Frequent updates of the calibration tables is much less critical for reprocessing activities because dedicated tables can be generated for selected periods outside the operational production chain.

In the previous section, Aeolus data from December 2019 were used for the characterization of the nonlinearity of the Mie spectral response which was next applied to Aeolus data of the same month to derive the corrected Mie-cloudy winds. Here we test the stability of this

procedure by applying the Mie nonlinearity correction of Figure 1 to Aeolus data of another period, namely the first week of November 2019, which counted a total of 264,764 Mie-cloudy winds. The reprocessed dataset, representative of the operational product, (with Mie nonlinearity correction based on the blue curve in Figure 1) showed ($o - b$) statistics similar to Figure 2 (but not shown) but with an overall bias of $-0.19 \text{ m}\cdot\text{s}^{-1}$, a standard deviation of $4.04 \text{ m}\cdot\text{s}^{-1}$ and scaled MAD value of $3.63 \text{ m}\cdot\text{s}^{-1}$. The corrected Mie-cloudy winds (with Mie nonlinearity correction based on the black crosses in Figure 1) has an overall bias of $-0.05 \text{ m}\cdot\text{s}^{-1}$, a standard deviation of $3.91 \text{ m}\cdot\text{s}^{-1}$ and scaled MAD value of $3.51 \text{ m}\cdot\text{s}^{-1}$, that is, an overall improvement relative to the operational product. In addition the wind speed-dependent bias and systematic bias near zero wind speed (“wiggling”) have been removed (Figure 9).

These results show that the NWP-based Mie nonlinearity correction does not only apply to the period for which it was derived, but the apparent stability of the nonlinear characteristics of the Mie spectral response allows the use for another period of Aeolus Level-2B processing as well, which is important for operational use as discussed in the beginning of this section. Monitoring of the Mie nonlinearity correction over the six-month period mid-April until mid-October 2021 did not reveal any significant divergence (not shown).

6 | SUMMARY AND DISCUSSION

The use of NWP data for monitoring the quality of retrieved Aeolus Mie-cloudy winds has proven very successful. It has revealed systematic errors in the (until June 2021) operational and disseminated Mie-cloudy wind product, which could be traced back to imperfections in the calibration tables which serve as input for the Aeolus Level-2B wind processing algorithms. The conclusion at this stage of the mission is that the preferred option of absolute instrument calibration has proven less successful than anticipated before launch. This can be explained by the fact that the emitted laser energy and optical efficiency of the instrument are less than anticipated before launch, meaning that the SNR of the received signal on the ACCD is less than anticipated before launch. As a consequence, instrument response calibration (IRC) is limited to global areas with large albedo, mainly polar regions, to allow for surface returns with sufficient SNR. Cloud obstruction causes data gaps which during calibration activities further limit calibration capabilities. In addition it is noted that IRC is performed in nadir-pointing mode, while wind measurements are performed in off-nadir. This results in different illumination of the spectrometers

due to differences in temperature gradient of the primary mirror. Due to this strong influence of the primary mirror telescope functions on the instrument responses (Weiler *et al.*, 2021), the nadir-pointing IRCs are not as representative as anticipated before launch for the use of instrument response calibrations.

As an alternative approach, the use of NWP model wind data for calibration purposes has been assessed and demonstrated successfully. The power of the method is that each Aeolus-retrieved wind has a NWP counterpart. As such, the use of NWP for calibration is not limited to polar regions and allows continuous monitoring of the instrument performance. The full global coverage allows a large data sample to characterize the instrument. In this paper the focus has been on characterizing the nonlinearity part of the Mie spectral response, but could in principle be extended to the linear part as well. Although this has not been investigated, it would imply there is no need for the instrument to be operated in calibration mode (nadir-pointing) for Mie channel characterization. As a consequence, no wind observations are lost due to calibration activities. It is also noted that IRC calibrations have not been performed at all for most of 2020 and the first half of 2021 because of concerns about the thermal effect of rotating the satellite. The NWP calibration method allows us to also get a good calibration for this period, which will certainly benefit upcoming datasets from reprocessing activities.

The use of the calibration tables, based on NWP calibration, as part of the Level-2B wind processing has removed systematic errors in retrieved Mie-cloudy winds, visually the wiggling effect. In addition, biases were reduced by $0.22 \text{ m}\cdot\text{s}^{-1}$ and the standard deviation by about 5%. There is no indication that NWP calibration draws retrieved winds too close toward NWP model winds, which would be detrimental for the use of these observations in data assimilation as part of NWP, as data assimilation explicitly assumes model and observation errors to be uncorrelated. High-resolution aircraft data from Mode-S EHS were used as an independent referee to further support the evidence that systematic errors revealed from observation versus model intercomparison could be attributed to observation errors; these were removed when using calibration tables from NWP calibration as part of Aeolus Mie-cloudy wind processing. A more sophisticated analysis for error attribution based on triple collocation (Stoffelen, 1998) is outside the scope of this study, but will be performed by our colleagues from the Institute of Marine Sciences (ICM) in Barcelona (Spain) in collaboration with the authors.

For operational use of the NWP-based calibration tables in the Level-2B processing, it is important that the frequency of the need to update the tables is low, say in the

order of months. The frequency of updating the calibration tables depends on the stability of the performance of the instrument over time. A stable instrument does not require frequent table updates. As mentioned above, NWP calibration allows for continuous monitoring of the instrument characteristics and hence the stability of the instrument performance over time.

Based on the presented results, the NWP-based calibration tables, as part of the Level-2B wind processing, have become part of the operational processing chain since 01 July 2021.

ACKNOWLEDGEMENTS

This research is funded by the European Space Agency (ESA) in the framework of the activities of the Aeolus DISC (Data Innovation and Science Cluster) consortium. The presented work includes reprocessed data from the first reprocessing activity which covered the June–December 2019 period. Upcoming reprocessing activities will include calibration tables based on the presented NWP calibration method to yield improved quality Mie-cloudy winds. The processor development, improvement and reprocessing activities are performed by the Aeolus DISC, which involves DLR, DoRIT, ECMWF, KNMI, CNRS, S&T, ABB and Serco, in close cooperation with the Aeolus PDGS. It should be noted that the idea of NWP calibration is predominantly based on many years of experience in scatterometer ocean-surface wind processing at KNMI and applied to Aeolus by Gert-Jan Marseille. The remaining co-authors contributed significantly by their detailed knowledge on Aeolus calibration procedures and the implementation of the presented method in the operational version of the Level-2B processor. Thanks to the many experts from the DISC and from ESA, who provided a fruitful forum for discussion during the Aeolus mission so far.

The authors are also grateful to Federico Cossu from the Institute of Marine Sciences (ICM) in Barcelona (Spain) for his effort of collocating high-resolution aircraft wind data from Mode-S EHS to Aeolus winds. The resulting dataset of collocated HLOS winds from Aeolus, ECMWF and Mode-S has proven very valuable and will be further used in error attribution studies based on the triple collocation technique.

AUTHOR CONTRIBUTIONS

Gert-Jan Marseille: conceptualization; data curation; formal analysis; investigation; methodology; project administration; resources; software; supervision; validation; visualization; writing – original draft; writing – review and editing. **Jos Klooe:** software; validation; visualization. **Uwe Marksteiner:** conceptualization; formal analysis; methodology. **Oliver Reitebuch:**

conceptualization; formal analysis; funding acquisition; investigation; methodology. **Michael Rennie:** conceptualization; formal analysis; methodology; validation. **Siebrren Haan:** formal analysis; investigation; validation.

ORCID

Gert-Jan Marseille  <https://orcid.org/0000-0003-4999-693X>

REFERENCES

- Baker, W.E., Emmitt, G.D., Robertson, F., Atlas, R.M., Molinari, J.E., Bowdle, D.A., Paegle, J., Hardesty, R.M., Menzies, R.T., Krishnamurti, T.N., Brown, R.A., Post, M.J., Anderson, J.R., Lorenc, A.C. and McElroy, J. (1995) Lidar-measured winds from space: a key component for weather and climate prediction. *Bulletin of the American Meteorological Society*, 76, 869–888. [https://doi.org/10.1175/1520-0477\(1995\)076<0869:LMWFSA>2.0.CO;2](https://doi.org/10.1175/1520-0477(1995)076<0869:LMWFSA>2.0.CO;2).
- Baker, W.E., Atlas, R., Cardinali, C., Clement, A., Emmitt, G.D., Gentry, B.M., Hardesty, R.M., Källén, E., Kavaya, M.J., Langland, R., Ma, Z., Masutani, M., McCarty, W., Pierce, R.B., Pu, Z., Riishøjgaard, L.P., Ryan, J., Tucker, S., Weissmann, M. and Yoe, J.G. (2014) Lidar-measured wind profiles: the missing link in the global observing system. *Bulletin of the American Meteorological Society*, 95, 543–564. <https://doi.org/10.1175/BAMS-D-12-00164.1>.
- de Haan, S. (2011) High-resolution wind and temperature observations from aircraft tracked by Mode-S air traffic control radar. *Journal of Geophysical Research*, 116. <https://doi.org/10.1029/2010JD015264>.
- de Haan, S. (2015) Estimates of Mode-S EHS aircraft-derived wind observation errors using triple collocation. *Atmospheric Measurement Techniques*, 9, 4141–4150. <https://doi.org/10.5194/amt-d-9-4141-2016>.
- Eyre, J.R. (1992) A bias correction scheme for simulated TOVS brightness temperatures. Technical Memorandum 176, Reading, UK: ECMWF.
- ESA (2008) ADM-Aeolus Science Report, SP-1311. Noordwijk, Netherlands: ESA.
- ESA (2016) ADM-Aeolus Mission Requirements Document, AE-RP-ESA-SY-001. Noordwijk, Netherlands: ESA.
- Lange, H. and Janjić, T. (2016) Assimilation of mode-S EHS aircraft observations in COSMO-KENDA. *Monthly Weather Review*, 144(5), 1697–1711.
- Lux, O., Wernham, D., Bravetti, P., McGoldrick, P., Lecrenier, O., Riede, W., D'Ottavi, A., De Sanctis, V., Schillinger, M., Lochard, J., Marshall, J., Lemmerz, C., Weiler, F., Mondin, L., Ciapponi, A., Kanitz, T., Elfving, A., Parrinello, T. and Reitebuch, O. (2020) High-power and frequency-stable ultraviolet laser performance in space for the wind lidar on Aeolus. *Optics Letters*, 45(6), 1443–1446. <https://doi.org/10.1364/OL.387728>.
- Lux, O., Lemmerz, C., Weiler, F., Kanitz, T., Wernham, D., Rodrigues, G., Hyslop, A., Lecrenier, O., McGoldrick, P., Fabre, F., Bravetti, P., Parrinello, T. and Reitebuch, O. (2021) ALADIN laser frequency stability and its impact on the Aeolus wind error. *Atmospheric Measurement Techniques*, 14, 6305–6333. <https://doi.org/10.5194/amt-14-6305-2021>.
- Marksteiner, U. (2013) *Airborne wind Lidar observations for the validation of the ADM-Aeolus instrument*. PhD thesis, Technische Universität München, Germany.

- Reitebuch, O. (2012) Wind lidar for atmospheric research, pp. 487–507 in *Atmospheric physics; research topics in aerospace*, editor=Schumann, U. Berlin: Springer.
- Reitebuch, O., Huber, D. and Nikolaus, I. (2018) ADM-Aeolus Algorithm Theoretical Basis Document (ATBD) level-1B products, AE-RP-DLR-L1B-001, issue 4.4 <https://earth.esa.int/eogateway/missions/aeolus/data>; accessed 13 January 2022.
- Rennie, M. (2016) TN16: advanced monitoring of Aeolus winds. Contract Report AE-TN-ECMWF-GS-16 to ESA, Reading, UK: ECMWF.
- Rennie, M. and Isaksen, L. (2020) The NWP impact of Aeolus level-2B winds at ECMWF. Technical Memorandum 864, Reading, UK: ECMWF.
- Rennie, M., Isaksen, L., Weiler, F., De Kloe, J., Kanitz, T. and Reitebuch, O. (2021) The impact of Aeolus wind retrievals in ECMWF global weather forecasts. *Quarterly Journal of the Royal Meteorological Society*, 147, 3555–3586. <https://doi.org/10.1002/qj.4142>.
- Stoffelen, A. (1998) Toward the true near-surface wind speed: error modeling and calibration using triple collocation. *Journal of Geophysical Research*, 103(C4), 7755–7766. <https://doi.org/10.1029/97JC03180>.
- Stoffelen, A., Pailleux, J., Källén, E., Vaughan, J.M., Isaksen, L., Flamant, P., Wergen, W., Andersson, E., Schyberg, H., Culoma, A., Meynard, R., Endemann, M. and Ingmann, P. (2005) The atmospheric dynamics mission for global wind field measurement. *Bulletin of the American Meteorological Society*, 86, 73–88. <https://doi.org/10.1175/BAMS-86-1-73>.
- Stoffelen, A., Benedetti, A., Borde, R., Dabas, A., Flamant, P., Forsythe, M., Hardesty, M., Isaksen, L., Källén, E., Körnich, H., Lee, T., Reitebuch, O., Rennie, M., Riishøjgaard, L.P., Schyberg, H., Straume, A.G. and Vaughan, M. (2020) Wind profile satellite observation requirements and capabilities. *Bulletin of the American Meteorological Society*, 101, E2005–E2021. <https://doi.org/10.1175/BAMS-D-18-0202.1>.
- Straume, A.G., Rennie, M., Isaksen, L., de Kloe, J., Marseille, G.-J., Stoffelen, A., Flament, T., Stieglitz, H., Dabas, A., Huber, D., Reitebuch, O., Lemmerz, C., Lux, O., Marksteiner, U., Weiler, F., Witschas, B., Meringer, M., Schmidt, K., Nikolaus, I., Geiss, A., Flamant, P., Kanitz, T., Wernham, D., Bismarck, J., von Bley, S., Fehr, T., Floberghagen, R. and Parinello, T. (2020) ESA's space-based Doppler Wind Lidar Mission Aeolus – first wind and aerosol product assessment results. *EPJ Web of Conferences*, 237. <https://doi.org/10.1051/epjconf/202023701007>.
- Tan, G.H., Andersson, E., de Kloe, J., Marseille, G.-J., Stoffelen, A., Poli, P., Denneulin, M.-L., Dabas, A., Huber, D., Reitebuch, O., Flamant, P., Le Rille, O. and Nett, H. (2008) The ADM-Aeolus wind retrieval algorithms. *Tellus A: Dynamic Meteorology and Oceanography*, 60(2). <https://doi.org/10.1111/j.1600-0870.2007.00285.x>.
- Weiler, F., Rennie, M., Kanitz, T., Isaksen, L., Checa, E., de Kloe, J., Okunde, N. and Reitebuch, O. (2021) Correction of wind bias for the lidar on board Aeolus using telescope temperatures. *Atmospheric Measurement Techniques*, 14, 7167–7185. <https://doi.org/10.5194/amt-14-7167-2021>.
- WMO (2018) Rolling Review of Requirements and Statements of Guidance. Available at: <https://community.wmo.int/oscar-wmo-observational-requirements-and-capabilities>, and OSCAR database https://space.oscar.wmo.int/variables/view/wind_horizontal.

How to cite this article: Marseille, G.-J., de Kloe, J., Marksteiner, U., Reitebuch, O., Rennie, M. & de Haan, S. (2022) NWP calibration applied to Aeolus Mie channel winds. *Quarterly Journal of the Royal Meteorological Society*, 1–15. Available from: <https://doi.org/10.1002/qj.4244>